Progress In Electromagnetics Research, Vol. 151, 151–167, 2015

Lossy Spherical Cavity Resonators for Stress-Testing Arbitrary 3D Eigenmode Solvers

Stergios Papantonis[1, 2] and Stepan Lucyszyn[1, 2, *]

Abstract—A lossy metal-wall cavity resonator that extends well beyond perturbation theory limits is studied. An exact analytical solution is employed for the spherical cavity resonator, having walls transformed from being a perfect electrical conductor (PEC) to free space. This model then acts as an ideal benchmark reference standard. A plane-wave approximation is then derived. Independent full-wave numerical modeling of the spherical cavity resonator is undertaken using eigenmode solvers within two well-known commercial, industry-standard, simulation software packages (HFSS^{TM}and COMSOL). It has been found that the plane-wave approximation model accurately characterizes the results generated by these solvers when equivalent finite conductivity boundary (FCB) and layered impedance boundary (LIB) conditions are used. However, the impedance boundary (IB) condition is accurately characterized by the exact model, but the precise value of complex wave impedance at the wall boundary for the specific resonance mode must first be known *a priori*. Our stress-testing results have profound implications on the usefulness of these commercial solvers for accurately predicting eigenfrequencies of lossy arbitrary 3D structures. For completeness, an exact series RLC equivalent circuit model is given specifically for a spherical cavity resonator having arbitrary wall losses, resulting in the derivation of an extended perturbation model.

1. INTRODUCTION

Electromagnetic cavity resonators having electrically conducting walls have been exploited for well over seven decades [1–3], because of their ability to produce sharp spectral resonances — much sharper than their lumped-element counterparts. Their ability to store electromagnetic energy with very low dissipative losses, from sub-microwave [4] to optical [5] frequencies, has made them an essential component in many systems. Spherical cavity resonators have the highest quality factor, when compared to rectangular or cylindrical cavities when made with the same wall material [6]. In general, it is highly desirable to have low-loss electromagnetic resonators (e.g., to implement high-performance impedance matching networks and filters) [7, 8]. However, there are many examples where very lossy resonant structures exist; requiring a more rigorous approach to the modeling of their behavior. Examples include: (1) surface plasmon polaritons, found in nature and engineered [9]; (2) heavy time-domain damping of unwanted resonances (e.g., in DC biasing networks) and even in control systems; (3) implementation of ultra wideband frequency-domain networks (e.g., antennas, phase shifters and filters found in ultra-high speed telecommunications and radar systems); (4) unexpected box-mode resonances with low-cost plastic/organic packaging of high frequency devices; (5) certain metamaterial and graphene structures; and (6) Shumann resonances in the spherical earth-ionosphere cavity.

Clearly, there is an inherent need for the accurate numerical simulation of arbitrary 3D structures, regardless of the levels of associated material losses. An illustrative example is that of metamaterials of

Received 17 March 2015, Accepted 12 May 2015, Scheduled 24 May 2015

* Corresponding author: Stepan Lucyszyn (s.lucyszyn@imperial.ac.uk).

[1] Optical and Semiconductor Devices Group, Department of Electrical and Electronic Engineering, Imperial College London, Exhibition Road, SW7 2AZ, United Kingdom. [2] Centre for Terahertz Science and Engineering, Imperial College London, Exhibition Road, SW7 2AZ, United Kingdom. Both authors contributed equally to this work.

infinite extent — an area that has received great interest in recent years — where full-wave numerical simulations often provide the only realistic option to study their behavior [10].

While structures with "good electrical conductors" can be easily modeled, and with excellent accuracy, this is not straightforward when low conductivity materials are modeled, as will be shown later. Commercial eigenmode solvers have never been stress-tested for their use with lossy materials. Indeed, the stress-testing of commercial electromagnetic full-wave simulation software packages is of critical importance to both the academic community and industry; as previously undertaken for the modeling of electrically-thin metal-walled structures [11] and those intended for use at terahertz frequencies [12]. To this end, a traceable benchmark structure (mathematically defined by an exact analytical model) is required, to compare its results with those from numerical simulations, with a view to quantifying levels of accuracy. With numerical electromagnetic field solvers intended for arbitrary 3D structures, the spherical cavity resonator represents an ideal benchmark structure. This is because, unlike lossy metal-walled rectangular cavity resonators, it does not suffer from the effects of diffraction; thus, it is able to provide an exact analytical solution for arbitrary levels of loss.

Low loss performance with metal-walled cavities is achieved with "good electrical conductors". Fortunately, in this case, the analysis can be greatly simplified with the use of approximate solutions (e.g., traditional perturbation techniques); this is well documented in many works (e.g., Slater [13]), but their validity is limited to low losses. A more general approach for the modeling of metal-walled cavities was reported by Hadidi and Hamid, for cylindrical resonators having lossy end walls; although their work still requires the use of approximations [14]. However, the exact analytical formulation for the generic case of a dielectric sphere inside another dielectric of infinite thickness was given by Gastine et al. in 1967 [15]. In their paper, the model was used to investigate the modal behavior of ideal lossless homogeneous dielectric spheres in free space.

To the best of our knowledge, after an exhaustive literature survey, the modeling of arbitrarily lossy metal-walled cavity resonators has not been reported. For this reason, the generic modeling of lossy metal-walled spherical cavity resonators is given here. Our analysis gives new insight into their behavior and, as a unique application, helps practitioners to perform stress-testing of their arbitrary 3D eigenmode solvers; by increasing the level of intrinsic loss within the conducting wall medium to any value (from zero to infinity).

2. EXACT ANALYTICAL FORMULATION

2.1. Generic Spherical Cavity Resonator

The electromagnetic fields within a spherical cavity are first expanded into normal waveguide modes. As is well known, the fields within the cavity can be decomposed into two families; namely, the transverse electric (TE) and transverse magnetic (TM). In our case, radially propagating waves with both families are of interest and, hence, so are the associated modes that are transverse with respect to the radial direction. In the general case of an inhomogeneous dielectric-filled cavity (along the radial direction) the modes are neither pure TE nor pure TM, but a superposition of both. One way to obtain the field distributions for each family is with the use of Hertz vector potentials. A thorough study of this method is beyond the scope of this work and can be found in classical electromagnetics textbooks [6, 16]. For example, using the expressions for the fields from [15], the transverse wave impedance for the transverse magnetic mode Z_{TM} can be written as

$$Z_{\mathrm{TM}}\left(\tilde{\beta}_{d,c}r\right) = \frac{E_\theta}{H_\varphi} = \begin{cases} j\eta_d \left[\dfrac{j_{n-1}\left(\tilde{\beta}_d r\right)}{j_n\left(\tilde{\beta}_d r\right)} - \dfrac{n}{\tilde{\beta}_d r}\right], & r < R_a \quad (1a) \\ j\eta_c \left[\dfrac{h^{(2)}_{n-1}\left(\tilde{\beta}_c r\right)}{h^{(2)}_n\left(\tilde{\beta}_c r\right)} - \dfrac{n}{\tilde{\beta}_c r}\right], & r > R_a \quad (1b) \end{cases}$$

where E_θ is the electric field associated with polar angle θ and H_φ is the magnetic field associated with azimuthal angle φ. Also, $j_n(x)$ and $h^{(2)}_n(x)$ are the nth-order spherical Bessel function of the first kind

and Hankel function of the second kind, respectively. In addition, $\eta_d = \sqrt{\mu_d/\varepsilon_d}$ and $\eta_c = \sqrt{\mu_c/\varepsilon_c}$ are the intrinsic impedances of the spherical cavity's internal dielectric filler and infinitely thick conducting wall materials, respectively, $\tilde{\beta}_d = \tilde{\omega}_0\sqrt{\mu_d\varepsilon_d}$, $\tilde{\beta}_c = \tilde{\omega}_0\sqrt{\mu_c\varepsilon_c}$ and the complex angular resonance frequency (or eigenfrequency) is given by $\tilde{\omega}_0 = \omega_0' + j\omega_0''$. Here, r is the radial coordinate and R_a is the radius of the cavity. Also for the conducting wall material, μ_c and $\varepsilon_c = \varepsilon_0(\varepsilon_{r\infty} - j\frac{\sigma_c}{\omega\varepsilon_0})$ are the effective permeability and effective permittivity, respectively, where ε_0 is the permittivity of free space and σ_c is the intrinsic conductivity. In this work, for convenience, we set $\mu_c = \mu_0$ (permeability of free space), $\varepsilon_{r\infty} = 1$ and $\sigma_c = \sigma_0$ (bulk DC conductivity). An example of a "good electrical conductor" is when $\sigma_0 \gg \omega\varepsilon_0$. This classical skin-effect approach for non-magnetic materials gives accurate results for the frequencies of interest (i.e., below *ca.* 1 THz [12, 17]). However, other material frequency dispersion models can also be easily employed [12, 17].

In order to obtain an unambiguous solution, the field components must satisfy the appropriate boundary conditions at the surface of the cavity wall (i.e., the tangential fields must be continuous at the wall surface); the transverse wave impedance must also be continuous across the wall interface. After some algebraic manipulations and using the relationship $f_n'(x) = f_{n-1}(x) - \frac{n+1}{x}f_n(x)$, where $f_n(x)$ is either the spherical Bessel function or Hankel function and the prime represents differentiation with respect to the argument, the following transcendental equation is obtained to meet the boundary condition for the TM_{mnp} modes, where m, n correspond to the variations along the azimuthal angle φ and polar angle θ, respectively, whereas p is associated with the variations along the radial direction.

$$\eta_d\left[\frac{j_{n-1}\left(\tilde{\beta}_d R_a\right)}{j_n\left(\tilde{\beta}_d R_a\right)} - \frac{n}{\tilde{\beta}_d R_a}\right] - \eta_c\left[\frac{h_{n-1}^{(2)}\left(\tilde{\beta}_c R_a\right)}{h_n^{(2)}\left(\tilde{\beta}_c R_a\right)} - \frac{n}{\tilde{\beta}_c R_a}\right] = 0 \tag{2}$$

For simplicity, and without any loss of generality, we focus our analysis on a dielectric-filled spherical cavity, where the two mode families are decoupled; operating in the dominant TM_{011} mode (i.e., $m = 0$, $n = p = 1$), although any other mode could also be studied. Moreover, we restrict our interest to mono-mode operation, in order to clearly illustrate physical behavior (i.e., without introducing additional complications from multi-mode effects). With the TM_{011} mode, the only non-zero field components are E_r, E_θ and H_φ.

2.2. Unloaded Quality Factor Definitions

For each value of σ_0 in turn, (2) is solved numerically for $\tilde{\omega}_0$. Each solution acts as a starting value for the next iteration, until convergence to a final solution is obtained. The eigenfrequencies are complex-valued because of the presence of losses associated with either the filler and/or wall materials. In the special case where the walls are lossless (i.e., perfect electric conductors (PEC) with $\eta_c = 0$) then (2) reduces to the standard textbook expression

$$j_1(\beta_I R_a) + \beta_I R_a j_1'(\beta_I R_a) = 0 \tag{3}$$

with the lowest resonant frequency given by $\beta_I R_a = 2.74370$ or equivalently by $\omega_I = 2.74370/(R_a\sqrt{\mu_d\varepsilon_d})$, where ω_I is the ideal angular resonance frequency (used as the initial starting value in the numerical solution of (2)).

By introducing a non-zero surface reactance, the undamped (or driven) angular resonance frequency $\omega_0 = |\tilde{\omega}_0|$ (normally associated with the steady-state frequency domain) is reduced from its value of ω_I. Moreover, the additional introduction of a non-zero surface resistance results in further frequency detuning; in general, shifting the actual angular resonance frequency down from ω_0 to the damped (or undriven) angular resonance frequency ω_0' [12] (normally associated with the transient time domain).

Once the complex eigenfrequency is obtained from (2), the unloaded quality factor of the resonator can be calculated from the standard definition

$$Q_u(\omega_R) = \omega_R\frac{W}{P_{loss}} \tag{4}$$

where W and P_{loss} are the time-average energy stored inside the cavity volume V and power dissipated/radiated at resonance, respectively, and ω_R is the resonance frequency (yet to be defined

unambiguously). After some straightforward calculations, taking into account that fields at resonance have $\mathbf{E}, \mathbf{H} \propto e^{j\tilde{\omega}_0 t} = e^{-\omega_0'' t} e^{j\omega_0' t}$, then (4) can be rewritten as

$$Q_u(\omega_R) = \frac{\omega_R}{2\omega_0''} \tag{5}$$

Now, the following question arises: at what angular resonance frequency ω_R should the unloaded quality factor be evaluated? With low loss resonant structures this is a trivial question, since $\omega_0 \cong \omega_0'$. However, with very lossy resonant structures, it is important to make the correct distinction. In the case where the driving source effectively compensates for all losses, the undamped angular resonance frequency is of interest and it is only meaningful to calculate the unloaded quality factor at $\omega_R = \omega_0$, as the oscillatory term. Alternatively, for the case where there is no driving source, the damped angular resonance frequency is of interest and the unloaded quality factor should only be evaluated at $\omega_R = \omega_0'$, as the oscillatory term. A more detailed discussion of this point will be given in Section 4, using a lumped-element RLC equivalent circuit model for the lossy spherical cavity resonator, and it will be shown how $Q_u(\omega_0')$ can be calculated from $Q_u(\omega_0)$.

3. MODELING APPROACHES, RESULTS AND DISCUSSION

3.1. Exact Analytical Results

The previous analysis is general and describes the behavior of a spherical cavity resonator made of arbitrary materials (both the filler and wall). Using (1), with an air-filled spherical cavity having an arbitrary radius $R_a = 150\,\mu\text{m}$, the transverse wave impedance for the transverse magnetic mode $Z_{TM}(\tilde{\beta}_{d,c} r)$ against radial distance for various intrinsic values of bulk DC wall conductivity is shown in Figure 1. For completeness, the corresponding electrical length of the cavity $\theta_{TM} = \Re\{\tilde{\beta}_{d,c} r\}$ is shown in Figure 2. It is interesting to see that as wall conductivity decreases electrical length also decreases. Also, a noticeable step change discontinuity at the wall boundary can be seen at 10 S/m but not 0.1 S/m. For our particular example, the transition between a dielectric and conducting wall can be considered when σ_0 is of the order of unity.

Equivalent to using (2), a 1D transmission line model for representing the spherical cavity resonator,

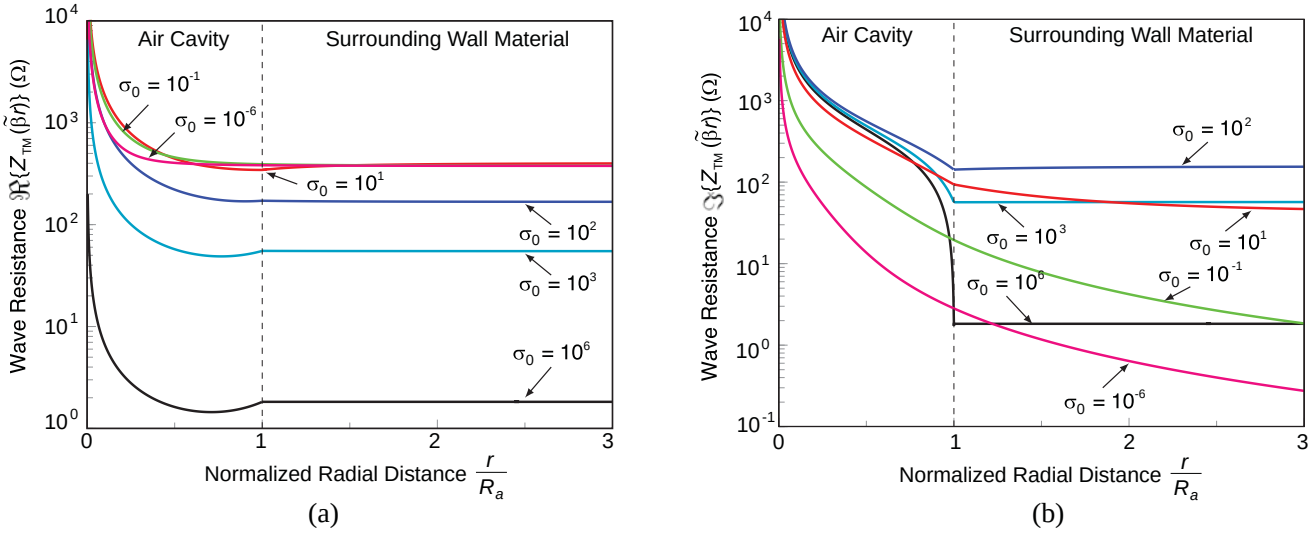

Figure 1. Wave impedance for the fundamental TM_{011} mode of an air-filled spherical cavity resonator having a 150 μm radius for various wall conductivities: (a) real part and (b) imaginary part.

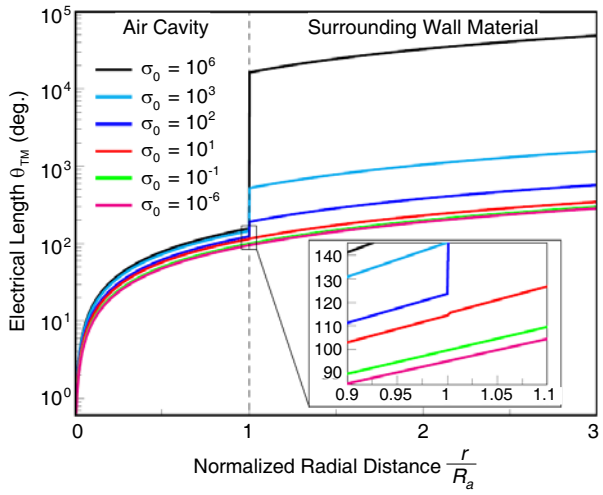

Figure 2. Electrical length for the fundamental TM_{011} mode of an air-filled spherical cavity resonator having a 150 µm radius for various wall conductivities.

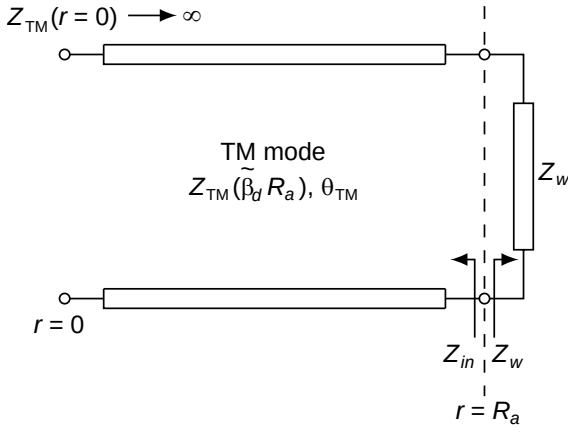

Figure 3. Transmission line model of the spherical cavity resonator at resonance.

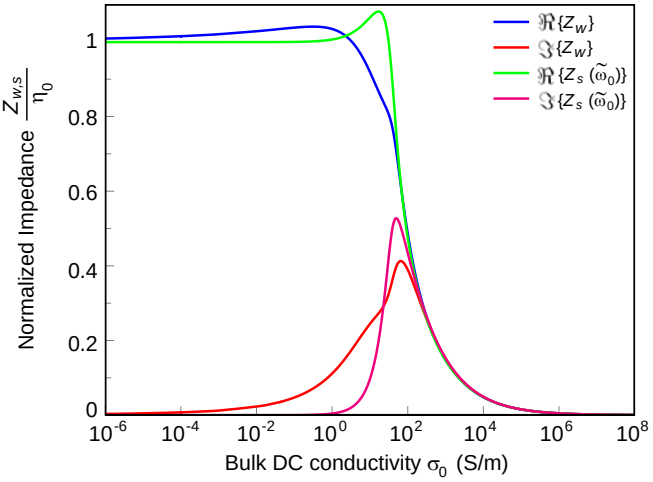

Figure 4. Wave and surface impedances at the complex resonant frequency $\tilde{\omega}_0$ at the wall boundary.

shown in Figure 3, can also be used to find the transverse resonance condition with

$$Z_{in} = Z_{\mathrm{TM}}\left(\tilde{\beta}_d R_a\right) \frac{Z_w + jZ_{\mathrm{TM}}\left(\tilde{\beta}_d R_a\right)\tan\left(\tilde{\beta}_d R_a\right)}{Z_{\mathrm{TM}}\left(\tilde{\beta}_d R_a\right) + jZ_w \tan\left(\tilde{\beta}_d R_a\right)} = Z_w \tag{6}$$

where $Z_{\mathrm{TM}}(\tilde{\beta}_d R_a)$ and Z_w are the modal impedances inside the cavity's volume given by (1a) and at the wall boundary given by (1b), respectively, with $r = R_a$. For completeness, wave impedance, calculated using (1), and surface impedance Z_s at the wall boundary are shown in Figure 4.

In this work, (2) is employed as a suitable benchmark reference standard to assess the performance of eigenmode solvers intended for arbitrary 3D structures. For the same resonator structure, the complex eigenfrequency $\tilde{f}_0 = f_0' + jf_0''$ and associated unloaded quality factors for intrinsic values of bulk DC wall conductivity of $10^{-6} \leq \sigma_0\,(\mathrm{S/m}) \leq 10^{+8}$, which effectively represents the transformation of the wall from being a PEC to free space, are shown in Figure 5.

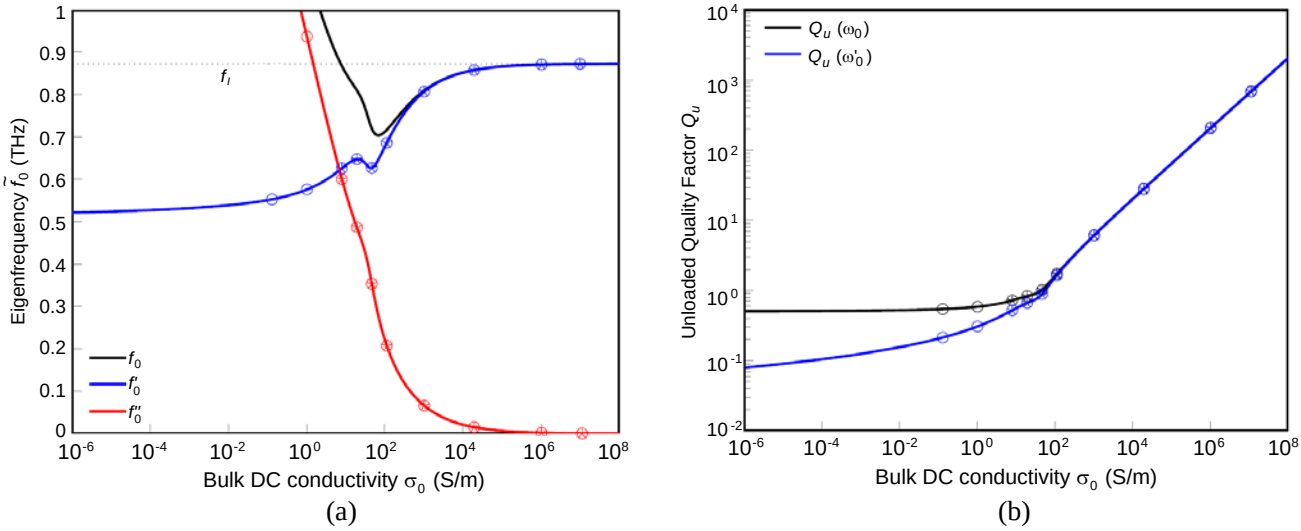

Figure 5. (a) Eigenfrequency for the fundamental TM_{011} mode of an air-filled spherical cavity resonator having a 150 µm radius; and (b) associated unloaded quality factors. Solid lines: Exact analytical results. Discrete symbols: numerical results obtained from commercial full-wave solvers (circles: HFSS^{TM} and stars: COMSOL).

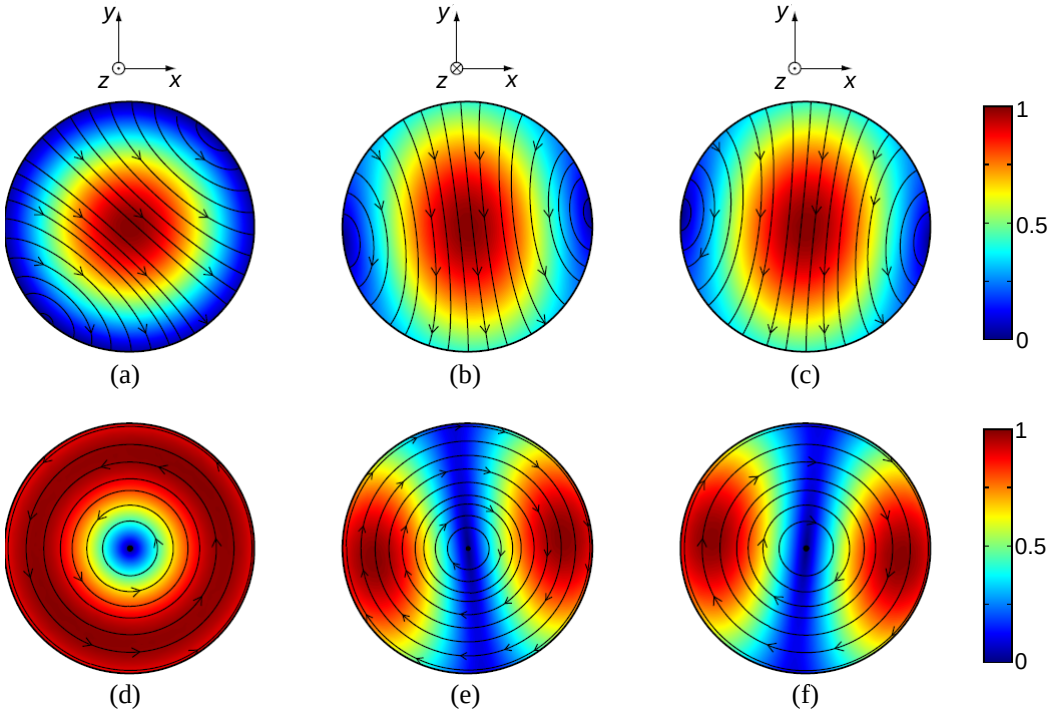

Figure 6. Normalized field patterns for the TM_{011} mode inside an air-filled spherical cavity resonator having a 150 µm radius, for the ideal case with $\sigma_0 \to \infty$ resulting in $f'_0 \to f_0 \to f_I = 0.8727$ THz. Electric field in (a) x-y, (b) x-z and (c) y-z plane. Magnetic field in (d) x-y, (e) x-z and (f) y-z plane.

Indeed, when taken to the free space limit of $\sigma_0 \to 0$, $\omega'_0 \to 0$ and, therefore, $\omega_0 \to \omega''_0 \to \infty$. This corresponds to the exponential decay of the fields having a time constant $\tau'' = 1/\omega''_0 \to 0$, i.e., a Dirac impulse response will be observed from a Dirac impulse excitation, as one would expect. Moreover, $Q_u(\omega_0) \to 0.5$ and $Q_u(\omega'_0) \to 0$, as the wall is transformed into free space (i.e., $Z_w(\sigma_0 \to 0) \to \eta_0$).

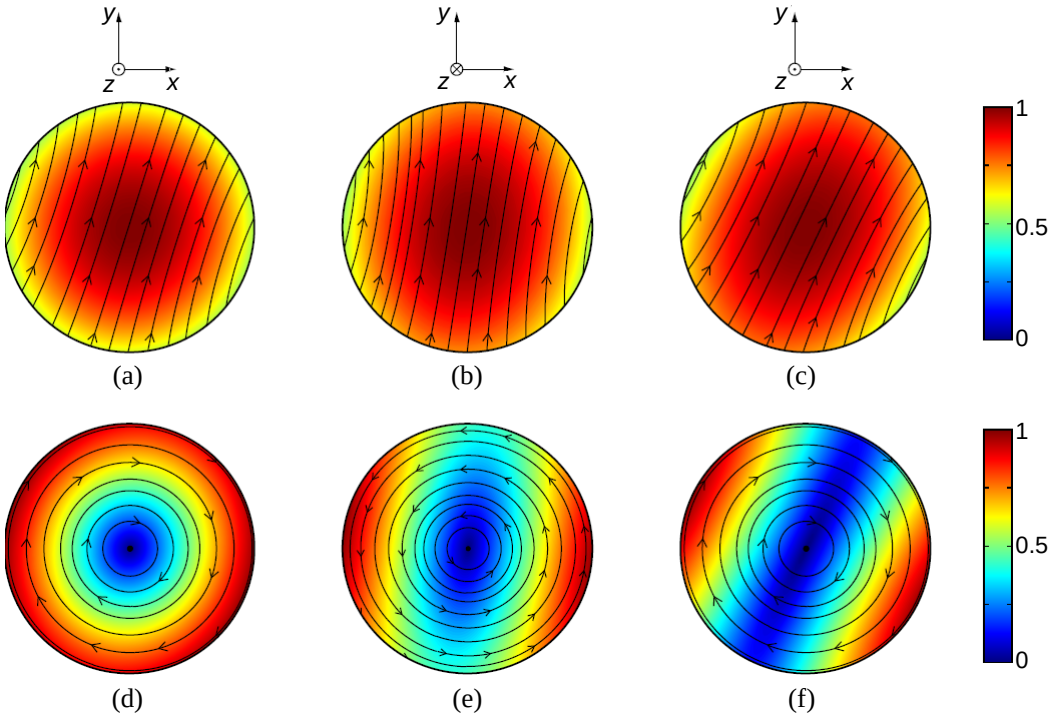

Figure 7. Normalized field patterns for the TM_{011} mode inside an air-filled spherical cavity resonator having a 150 µm radius, without neglecting the displacement current term, for the lossy case with $\sigma_0 = 65\,\mathrm{S/m}$. This results in $f_0' = 642.8\,\mathrm{GHz}$, $f_0 = 703.6\,\mathrm{GHz}$, $Q_u(\omega'_0) = 1.1$ and $Q_u(\omega_0) = 1.2$. Electric field in (a) x-y, (b) x-z and (c) y-z plane. Magnetic field in (d) x-y, (e) x-z and (f) y-z plane.

Table 1. Relaxation frequencies for various conducting wall materials at room temperature [18, 19] with the exact results.

Conductor	σ_0 (S/m)	τ (fs)	f_τ (THz)	f_0 (THz)
gold	4.1×10^7	27.135	5.87	0.872
ITO	$\sim 8 \times 10^5$	12.6	12.6	0.870
carbon	$\sim 10^3$	120	1.3	0.809

Clearly, the fundamental TM_{011} mode is theoretically supported for all air-filled spherical cavity resonators not having perfectly lossless walls (i.e., with $\sigma_0 > 0$).

The associated field patterns inside the cavity resonator are shown in Figure 6 for the PEC wall and Figure 7 for a very low conductivity wall.

It is worth mentioning that, with resonance frequencies below the wall material's phenomenological scattering relaxation frequency $f_\tau = 1/(2\pi\tau)$, where τ is the phenomenological scattering relaxation time, Drude relaxation effects can be ignored [12, 17]. For the air-filled cavity being considered here (having $R_a = 150\,\mu\mathrm{m}$ and $f_I = 0.8727\,\mathrm{THz}$) $f_0 < f_\tau$, as seen in Table 1 for three arbitrary conductors.

3.2. Analytical Plane-wave Approximation

In general, when simulating a structure having arbitrary materials, there are two approaches to defining its walls. The first is to physically draw each material region, as a 3D object, and then assign its bulk material parameters. Alternatively, the 3D regions can be replaced by a 2D surface boundary, where the appropriate material parameters are entered. A detailed study for low loss metal structures can be found in [12]. However, both of these approaches have weaknesses with low conductivity materials. For example, with the former approach, as the wall's bulk conductivity decreases, thicker walls are required

to achieve a constant skin depth thickness. Therefore, the wall thickness is a limiting factor. It has been found that when the intrinsic bulk DC conductivity of the wall is $\lesssim 50\,\mathrm{S/m}$, the eigenmode solver does not converge on a solution. On the other hand, when conductivity is $\gtrsim 10^5\,\mathrm{S/m}$, the computational resources and time required to mesh and solve inside the wall are impractical. As a result, this former approach can only be used within a relatively narrow bulk DC conductivity range.

For this reason, surface boundary conditions can be employed, for many applications, as a more efficient modeling approach; in extreme cases this is the only approach available. For example, with HFSS$^{\mathrm{TM}}$ (version 13) [20], there are three different boundary conditions available: Finite Conductivity Boundary (FCB), Layered Impedance Boundary (LIB) and Impedance Boundary (IB). With the first two, the user enters bulk material parameters (e.g., $\boldsymbol{\mu_r} \rightarrow \mu_c/\mu_0$, $\boldsymbol{\varepsilon_r} \rightarrow \varepsilon_{r\infty}$, $\boldsymbol{\sigma} \rightarrow \sigma_c$, where variables in bold are the software parameters to be entered) for the wall (similar to the solid object definition), whereas with IB the value of the complex surface impedance $\mathbf{Z}_s$ has to be entered (which must be known *a priori* [12]). Similarly, with COMSOL (version 4.3a) [21], either the FCB, LIB or IB conditions can be met by the suitable manipulation of the following formulation

$$\mathbf{Z}_s = \sqrt{\frac{\mu_0 \boldsymbol{\mu_r}}{\varepsilon_0 \boldsymbol{\varepsilon_r} - j\frac{\boldsymbol{\sigma}}{\omega}}} \tag{7}$$

With HFSS$^{\mathrm{TM}}$ (with the exception of IB) and COMSOL, the boundary conditions rely purely on the wall's bulk material parameters; suggesting that an approximation model can be derived to accurately predict the results generated by the solvers. It has been found that this can be achieved by equating the wave impedance Z_w to the wall's intrinsic impedance $\eta_c(\tilde{\omega}) = \sqrt{\frac{j\tilde{\omega}\mu_0}{\sigma_0 + j\tilde{\omega}\varepsilon_0}} \equiv Z_s(\tilde{\omega}) = R_s(\tilde{\omega}) + jX_s(\tilde{\omega})$, and using the Leontovich surface impedance boundary condition

$$\mathbf{E} \times \mathbf{u}_r|_{r=R_a} = Z_s\,(\mathbf{u}_r \times \mathbf{H}) \times \mathbf{u}_r|_{r=R_a} \tag{8}$$

In general, using (1b), the wave impedance at the interface ($r = R_a$) can be written as

$$Z_w = \left.\frac{E_\theta}{H_\varphi}\right|_{r=R_a} = j\eta_c \left[\frac{h_{n-1}^{(2)}\left(\tilde{\beta}_c R_a\right)}{h_n^{(2)}\left(\tilde{\beta}_c R_a\right)} - \frac{n}{\tilde{\beta}_c R_a}\right] \tag{9}$$

and, thus, with the relationship $\lim\limits_{x\to\infty}\{h_n^{(2)}(x)\} = j^{n+1}\frac{e^{-jx}}{x}$, the analytical plane-wave approximation (9), where $|\tilde{\beta}_c R_a| \rightarrow \infty$ is proposed. From (2), the characteristic equation for the plane-wave approximation for the TM_{011} mode is given by

$$\eta_d \left[\frac{j_0\left(\tilde{\beta}_d R_a\right)}{j_1\left(\tilde{\beta}_d R_a\right)} - \frac{1}{\tilde{\beta}_d R_a}\right] + j\eta_c = 0 \tag{10}$$

It will be shown that this model accurately predicts the results for both commercial eigenmode solvers. Similarly, from (9), the wave impedance at the boundary for the plane-wave approximation for the TM_{011} mode has the following asymptotic behavior

$$\lim_{|\tilde{\beta}_c R_a|\to\infty}\{Z_w\} = j\eta_c \lim_{|\tilde{\beta}_c R_a|\to\infty}\left\{\frac{h_0^{(2)}\left(\tilde{\beta}_c R_a\right)}{h_1^{(2)}\left(\tilde{\beta}_c R_a\right)} - \frac{1}{\tilde{\beta}_c R_a}\right\} = \eta_c \tag{11}$$

3.3. Plane-Wave Approximation and Numerical FCB Results

With the FCB condition in HFSS$^{\mathrm{TM}}$, as explained in the software Technical Notes, the displacement current term is neglected; thus, $Z_0 = R_0(1+j)$, with surface resistance $R_0 = \sqrt{\frac{\omega\mu_0}{2\sigma_0}}$ [12, 17]. While, with COMSOL, this model is obtained by setting $\boldsymbol{\mu_r} = 1$, $\boldsymbol{\varepsilon_r} = 0$ and $\boldsymbol{\sigma} = \sigma_0$. This approach is only valid for "good electrical conductors" and it will be seen that this has no physical meaning when conducting wall losses are high. This gross assumption is, however, the most widely used with traditional perturbation

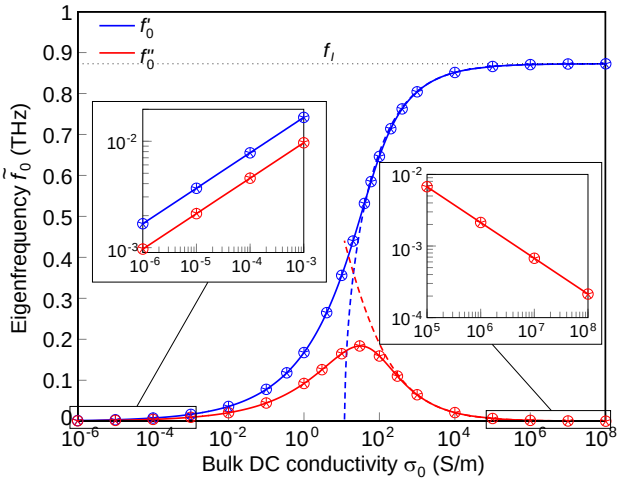

Figure 8. Eigenfrequency for the fundamental TM_{011} mode of the air-filled spherical cavity resonator having a 150 µm radius, neglecting the displacement current term. Solid lines: analytical plane-wave approximation results. Discrete symbols: numerical results obtained with full-wave solvers (circles: HFSS^{TM} and stars: COMSOL). Results from extended perturbation method are also shown with dashed lines (positive values for the damped resonance frequency f'_0 can only be given when $\sigma_0 \gtrsim 10$).

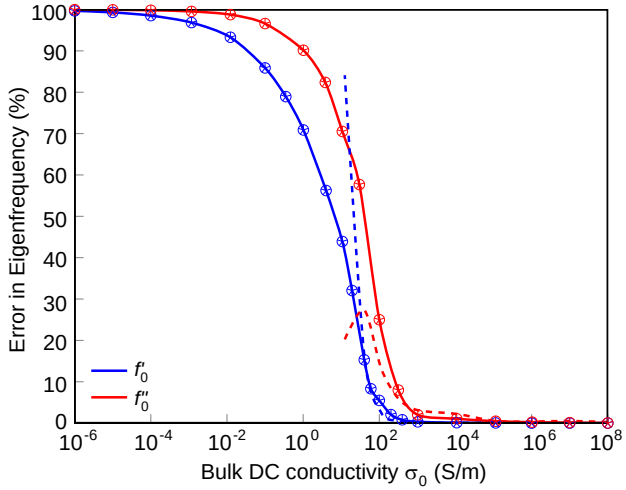

Figure 9. Percentage errors for eigenfrequencies using the FCB condition (circles: HFSS^{TM} and stars: COMSOL). The error from extended perturbation method is also shown with dashed lines.

methods [22]. Nevertheless, this classical skin-effect model, which excludes the displacement current term, will be used to determine eigenfrequencies as a means to validate our analytical plane-wave approximation model. To this end, Figure 8 and Figure 9 show the eigenfrequencies and associated percentage error, respectively, against intrinsic wall conductivity.

Although the results for low conductivity values lack physical meaning, the output data from commercial eigenmode solvers have been perfectly characterized using our plane-wave approximation model. It can be seen that the worst-case error for FCB is 100%.

3.4. Plane-wave Approximation and Numerical LIB Results

Next, the classical skin-effect model that includes both conduction and displacement current terms is considered; thus, $R_s \neq X_s$. With HFSS^{TM} this is obtained using the LIB condition, whereas with COMSOL this is the default boundary by setting $\boldsymbol{\mu_r} = 1$, $\boldsymbol{\varepsilon_r} = 1$ and $\boldsymbol{\sigma} = \sigma_0$. As seen in Figure 10, it has been found that this approach results in artificial cut-off values for conductivity $\sigma_{0c} \cong 2.46 \times 10^{-3}/R_a$ and associated undamped resonance frequency $f_{0c} \cong 82.01 \times 10^6/R_a$, below which the TM_{011} mode cannot be predicted. However, this is an artifact of the analytical plane-wave approximation and surface impedance models used. Therefore, this approach cannot generate any eigenfrequencies when the wall conductivity is lower that the cut-off value. The corresponding percentage errors with this approach are shown in Figure 11. As with FCB, the errors found with the LIB condition are unacceptable, reaching a value of $\sim 33\%$.

3.5. Unloaded Quality Factor Results for FCB and LIB

The unloaded quality factors at the driven and undriven resonance frequencies are shown in Figure 12. It is worth noting that the eigenmode solver in COMSOL can only report values of $Q_u(\omega'_0) = \frac{\omega'_0}{2\omega''_0} > 0.5$,

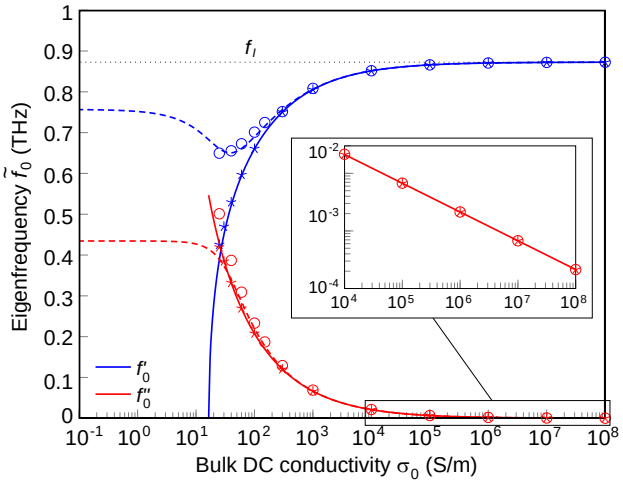

Figure 10. Eigenfrequency for the fundamental TM_{011} mode of the air-filled spherical cavity resonator having a 150 μm radius, without neglecting the displacement current term. Solid lines: analytical plane-wave approximation results (positive values for the damped resonance frequency f_0' can only be given when $\sigma_0 \geq \sigma_{0c}$). Discrete symbols: numerical results obtained with full-wave solvers (circles: HFSS^{TM} and stars: COMSOL). Results from extended perturbation method are also shown with dashed lines.

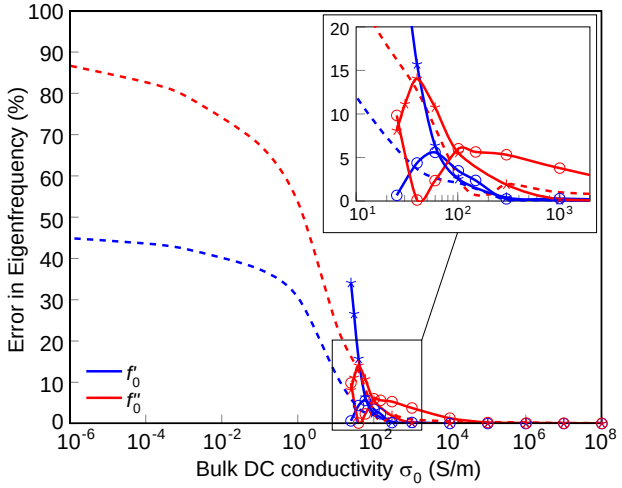

Figure 11. Percentage errors for eigenfrequencies using the LIB condition (circles: HFSS^{TM} and stars: COMSOL). The error from extended perturbation method is also shown with dashed lines.

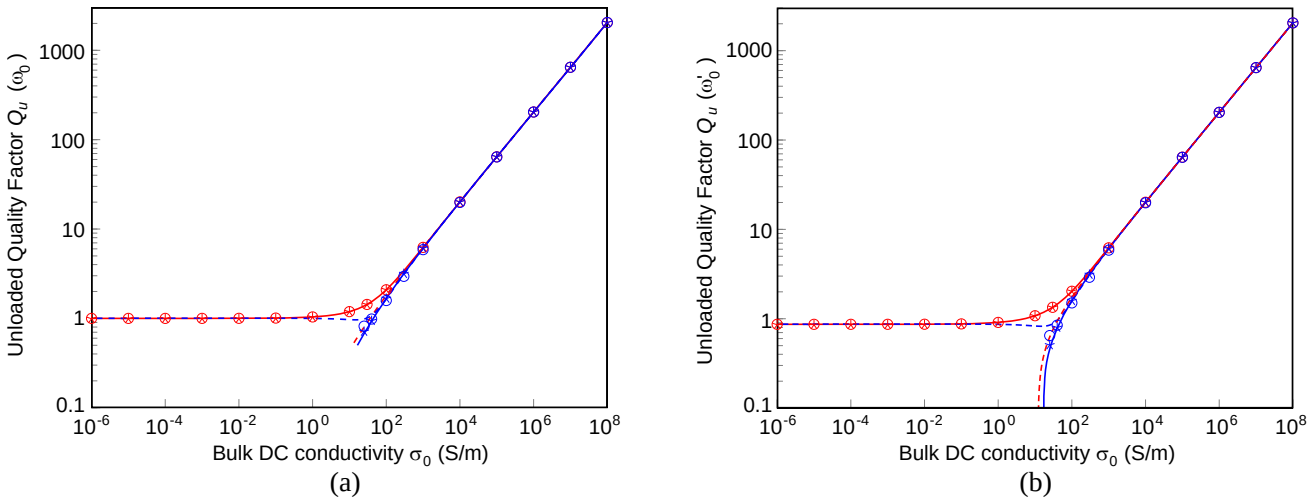

Figure 12. Unloaded quality factors: (a) $Q_u(\omega_0)$; and (b) $Q_u(\omega_0')$ for the fundamental TM_{011} mode of the air-filled spherical cavity resonator having a 150 μm radius, when neglecting the displacement current term (red) and without neglecting the displacement current term (blue), respectively. Solid lines: analytical plane-wave approximation results. Discrete symbols: numerical results obtained with full-wave solvers (circles: HFSS^{TM} and stars: COMSOL). Results from extended perturbation method are also shown with dashed lines.

which corresponds to $Q_u(\omega_0) = \frac{\omega_0}{2\omega_0'} > 1/\sqrt{2}$, regardless of the modeling approach.

The reason for the weaknesses when using both FCB and LIB conditions is that the wave impedance inherently depends on the geometry (since Z_w is a function of R_a) and, therefore, their accuracy is limited by this; geometry is not taken into account by the material input parameters $\boldsymbol{\mu_r}$, $\boldsymbol{\varepsilon_r}$ and $\boldsymbol{\sigma}$.

For example, when observing the wave impedance along the radial distance, as shown in Figure 1, it is clear that only for sufficiently high wall conductivities is the wave impedance constant within the wall and, hence, can be approximated by its intrinsic/surface impedance.

3.6. Exact Analytical and Numerical IB Results

With HFSS$^{\text{TM}}$, the IB condition allows the user to enter the complex surface impedance. This generally gives very accurate results, as shown in Figure 5. It is interesting to see that f_0' does not decrease monotonically with decreasing intrinsic conductivity (with a dip seen at $\sim 46\,\text{S/m}$). Also, f_0 can exceed f_I where quality factor is below unity, with a physical interpretation that is best observed in the time domain for such a highly damped condition.

Unfortunately, with HFSS$^{\text{TM}}$, the IB condition fails with very low intrinsic conductivity values of $\lesssim 0.1\,\text{S/m}$, as the solver cannot converge onto any solution. Similarly, with COMSOL, the user has to take into account (7) and define the material parameters so that (7) has a value equal to Z_w (by forcing $\boldsymbol{\mu_r} \to \frac{Z_w^2}{\mu_0}$, $\boldsymbol{\varepsilon_r} \to \frac{1}{\varepsilon_0}$ and $\boldsymbol{\sigma} \to 0$). Again, this solver can only converge when $Q_u(\omega_0') > 0.5$.

Moreover, with both HFSS$^{\text{TM}}$ and COMSOL solvers, *a priori* knowledge of the resonance frequency and the wave impedance at the boundary (i.e., the exact analytic expression given by (9)) is required; otherwise it will result in failure to predict the eigenfrequencies for arbitrary 3D structures having lossy conducting wall materials.

3.6.1. Perturbation Approximations

For completeness, perturbation methods have been included. The undamped resonance frequency ω_0 can be found by solving [23]

$$X_s(\omega_0) - 2(\omega_I - \omega_0)\Gamma = 0 \tag{12}$$

where, the geometrical factor for a spherical cavity is given by

$$\Gamma = \mu_0 \frac{\iiint_V H \cdot H^* dV}{\iint_S H_{\tan} \cdot H_{\tan}^* dS} = \frac{\mu_0}{\xi}\left(\frac{V}{S}\right) \tag{13}$$

and [24]

$$\xi = \frac{2}{3}\frac{(\beta_I R_a)^2 \sin^2(\beta_{\text{I}} R_a)}{1 - \left[1 + \frac{1}{(\beta_{\text{I}} R_a)^2}\right]\sin^2(\beta_{\text{I}} R_a)} \cong 0.90790$$

and

$$\left(\frac{V}{S}\right) = \frac{R_a}{3}$$

where suffix "tan" represents the field components tangential to the wall surface, $V = 4\pi R_a^3/3$ the internal cavity volume, and $S = 4\pi R_a^2$ the inner surface area of the wall. It is then trivial to calculate the corresponding unloaded quality factor from

$$Q_u(\omega_0) \sim \begin{cases} \dfrac{\omega_I \Gamma}{R_s(\omega_0)} \cong \dfrac{\eta_0}{R_s(\omega_0)} & \text{Traditional Perturbation} \quad (14a) \\ \dfrac{\omega_0 \Gamma}{R_s(\omega_0)} & \text{Extended Perturbation} \quad (14b) \end{cases}$$

where $\eta_0 = \sqrt{(\mu_0/\varepsilon_0)}$ is the intrinsic impedance of free space.

When comparing the results from all the various approaches, it is clear that they all approximate to the exact analytical solution in the low loss region (i.e., "good electrical conductor" behavior).

4. EXACT EQUIVALENT CIRCUIT MODELING FOR LOSSY SPHERICAL CAVITY RESONATORS

For a meaningful physical insight, it is convenient to interpret any resonator with a lumped-element RLC equivalent circuit model. This is particularly useful if characterizing resonators can be undertaken without the need for performing electromagnetic calculations.

4.1. Exact Solution

The cavity resonator can be regarded as an elementary resonant circuit, as shown in Figure 13(a), where the inductor and capacitor depend on the cavity filler (i.e., μ_d, ε_d), cavity size (e.g., R_a) and wall material (i.e., μ_0, ε_0, σ_0). All these parameters implicitly affect the complex natural resonance frequency $\tilde{\omega}_0$, as [25]

$$\tilde{\omega}_0 = \frac{1}{\sqrt{\tilde{L}_{eff}\tilde{C}_{eff}}} \tag{15}$$

$$\tilde{L}_{eff} = L' + jL'' = \mu_d V \tilde{\beta}_0^2 \tag{16}$$

$$\tilde{C}_{eff} = C' + jC'' = \frac{\varepsilon_d}{V}\frac{1}{\tilde{\beta}_0^4} \tag{17}$$

where, for an air-filled spherical cavity resonator, we obtain

$$L' = \mu_0 V \frac{\left(\omega_0'^2 - \omega_0''^2\right)}{c^2} \tag{18}$$

$$L'' = \mu_0 V \frac{2\omega_0'\omega_0''}{c^2} \tag{19}$$

$$C' = \frac{\varepsilon_0}{V}\left(\frac{c}{\omega_0^2}\right)^4 \left[\left(\omega_0'^2 - \omega_0''^2\right)^2 - \left(2\omega_0'\omega_0''\right)^2\right] \tag{20}$$

$$C'' = \frac{\varepsilon_0}{V}\left(\frac{c}{\omega_0^2}\right)^4 4\omega_0'\omega_0''\left(\omega_0''^2 - \omega_0'^2\right) \tag{21}$$

where $c = 1/\sqrt{(\mu_0\varepsilon_0)}$ is the speed of light in free space.

All parameters depend explicitly on both the real and imaginary parts of the complex eigenfrequency and implicitly on the intrinsic bulk DC conductivity of the wall (since it also affects the complex eigenfrequency).

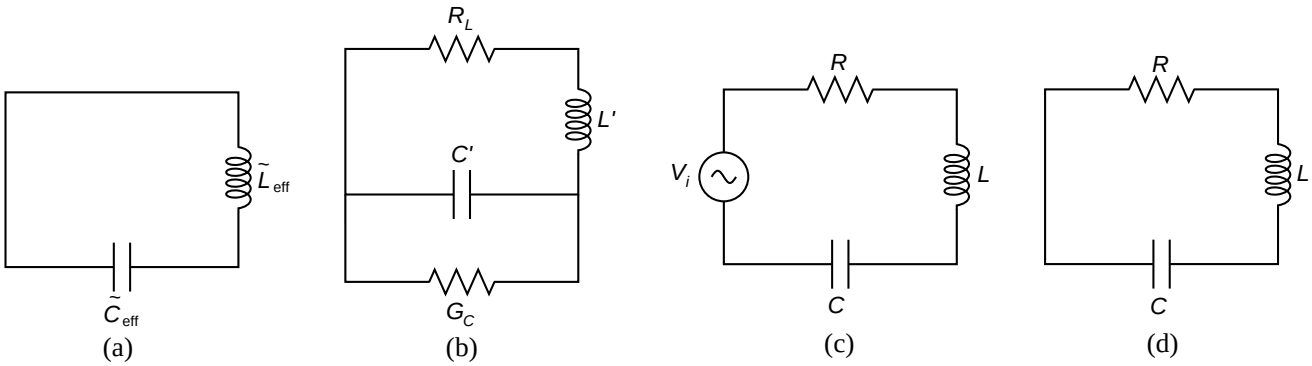

Figure 13. Lumped-element RLC equivalent circuit models for the fundamental TM_{011} mode: (a) elementary resonant circuit with complex effective inductance and capacitance; (b) resonant circuit after replacing the complex effective components with equivalent real components; (c) driven RLC circuit; and (d) undriven RLC circuit.

Although the resonant circuit in Figure 13(a) fully describes the behavior of the cavity at resonance it does not offer any meaningful physical insight, because of the complex nature of the effective inductance $\tilde{L}_{eff}$ and effective capacitance $\tilde{C}_{eff}$. Purely real components can be employed, as shown in Figure 13(b), having values derived using the following transformations

$$Z_{series} = j\omega_0 \tilde{L}_{eff} = R_L + j\omega_0 L' \quad \text{where} \quad R_L = -\omega_0 L'' \tag{22}$$

$$Y_{shunt} = j\omega_0 \tilde{C}_{eff} = G_C + j\omega_0 C' \quad \text{where} \quad G_C = -\omega_0 C'' \tag{23}$$

However, a meaningful physical insight is still not yet given, as individual component values can be negative. Instead, it is more traditional to represent the complex resonance behavior by an equivalent RLC network, as shown in Figure 13(c), where the driving source automatically compensates for the combined losses (represented solely by R) and, thus, the resonance frequency $\omega_0 = |\tilde{\omega}_0| = 1/\sqrt{LC}$ is purely real in this effectively lossless scenario. Moreover, with driven resonant circuits, the resistance R does not contribute to the detuning of the resonance frequency. This topology is widely used when characterizing tuned circuits, by measuring ω_0 and $Q_u(\omega_0) = \omega_0 L/R$ in the frequency domain.

As a result, using (19) with $\omega_R = \omega_0$, the lumped-element series RLC equivalent circuit components, all having positive values, can be expressed as

$$R\left(\tilde{\omega}_0\right) = 2\omega_0'' L\left(\omega_0\right) = \mu_0 V 2\omega_0'' \left(\frac{\omega_0}{c}\right)^2 \tag{24}$$

$$L\left(\omega_0\right) = \left|\tilde{L}_{eff}\right| = \mu_d V \left|\tilde{\beta}_0\right|^2 = \mu_0 V \left(\frac{\omega_0}{c}\right)^2 \tag{25}$$

$$C\left(\omega_0\right) = \left|\tilde{C}_{eff}\right| = \frac{\varepsilon_d}{V}\frac{1}{\left|\tilde{\beta}_0\right|^4} = \frac{\varepsilon_0}{V}\left(\frac{c}{\omega_0}\right)^4 \tag{26}$$

It should be noted that these equations give exact values that are fixed for each unique value of $\tilde{\omega}_0$ and must be frequency invariant (i.e., they cannot be frequency dispersive with $\omega \neq \tilde{\omega}_0$).

Removing the sinusoidal driving source gives Figure 13(d), where the combined losses cannot be compensated for. Therefore, in this lossy scenario, time-domain measurements with a Dirac impulse excitation would reveal the complex eigenfrequency, given by [23]

$$\tilde{\omega}_0 = \omega_0 \left[\sqrt{1 - \left(\frac{1}{2Q_u(\omega_0)}\right)^2} + j\frac{1}{2Q_u(\omega_0)}\right] \tag{27}$$

Therefore, with undriven resonant circuits, the resistance R contributes to further detuning of the resonance frequency from the undamped ω_0 down to the damped $\omega_0' = \sqrt{\omega_0^2 - (R/2L)^2}$. The topology in Figure 13(d) is also widely used when characterizing tuned circuits, by measuring ω_0' and the decay time constant $\tau'' = 2L/R$, in the time domain, which gives $Q_u(\omega_0') = \omega_0'\tau''/2 = \omega_0' L/R$.

It can be seen in (25) and (26) that L and C, respectively, are only a function of ω_0, which can be determined from frequency-domain simulations/measurements. In contrast, as seen in (24), R is a function of $\tilde{\omega}_0$ and, therefore, this and subsequently $Q_u(\omega_R)$ would normally require a numerical eigenmode solver or time-domain simulations/measurements (i.e., closed-form expressions cannot be used).

If the undamped resonance frequency and associated unloaded quality factor $Q_u(\omega_0)$ are known, using (27), one can calculate the damped resonance frequency and associated quality factor as follows

$$\left.\begin{aligned} \omega_0'' &= \frac{\omega_0}{2Q_u\left(\omega_0\right)} \\ \omega_0' &= \sqrt{\omega_0^2 - \omega_0''^2} \end{aligned}\right\} \longrightarrow Q_u\left(\omega_0'\right) = \frac{\omega_0'}{2\omega_0''} \tag{28}$$

Alternatively, after some basic algebraic manipulations, the following shows the generic transformation between unloaded quality factor definitions normally associated with both the frequency and time domains

$$Q_u\left(\omega_0'\right) = \sqrt{Q_u^2\left(\omega_0\right) - \left(\frac{1}{2}\right)^2} \tag{29}$$

This relationship is very important for low quality factor resonators, because it clearly shows that the unloaded Q-factors are fundamentally different for the driven and undriven cases (i.e., not equivalent, as often stated without qualification) and must be explicitly defined; whether it is applied to high loss resonator or heavily damped control system scenarios. For example, at the point of critical damping, $Q_u(\omega_0) = 0.5$ and, therefore, $Q_u(\omega_0') = 0$; otherwise with $Q_u(\omega_0') = 0.5$ then $Q_u(\omega_0) = 1/\sqrt{2}$; which is clearly an under-damped oscillatory condition.

Now, by re-arranging (28) and (29), the following expressions can be obtained

$$L(\omega_0) = \xi\Gamma\beta_0^2 S = \xi\Gamma\left(\frac{\omega_0}{c}\right)^2 4\pi R_a^2 \tag{30}$$

$$\therefore L(\omega_0) = L_I\left(\frac{\omega_0}{\omega_I}\right)^2 \quad \text{with} \quad L_I = \mu_0 V \beta_I^2 \tag{31}$$

and

$$C(\omega_0) = C_I\left(\frac{\omega_I}{\omega_0}\right)^4 \quad \text{with} \quad C_I = \frac{\varepsilon_0}{V}\frac{1}{\beta_I^4} \tag{32}$$

where $\omega_I = 1/\sqrt{(L_I C_I)}$.

Similarly, re-arranging (24), the following is found

$$R(\tilde{\omega}_0) = 2\omega_0''\xi\Gamma\beta_0^2 S \tag{33}$$

Using (13), it can be shown that

$$\omega_I\Gamma = \left(\frac{\beta_I R_a}{3\xi}\right)\eta_0 \cong 1.00734\eta_0 \tag{34}$$

As a result

$$R(\tilde{\omega}_0) = (\beta_I R_a)^3\left(\frac{8\pi}{3}\right)\left(\frac{\omega_0''\omega_0^2}{\omega_I^3}\right)\eta_0 \cong \frac{86.5165}{Q_u(\omega_0)}\left(\frac{\omega_0}{\omega_I}\right)^3\eta_0 \tag{35}$$

It is interesting to show the exact values at resonance for the lumped-element RLC equivalent circuit components given in Figure 13(d) and surface impedance $Z_s(\omega_0)$, against intrinsic wall conductivity, as seen in Figure 14. The unusual dip in f_0, seen in Figure 2(a), corresponds to the sharp peak in $C(\omega_0)$ at $\sim 72\,\mathrm{S/m}$; this also corresponds to the slight dip in $L(\omega_0)$, turning point in $R_s(\omega_0)$ and peak in $X_s(\omega_0)$. The similar uncharacteristic dip in f_0' at $\sim 46\,\mathrm{S/m}$ is the result of the interaction of ω_0 and ω_0'', governed by (28).

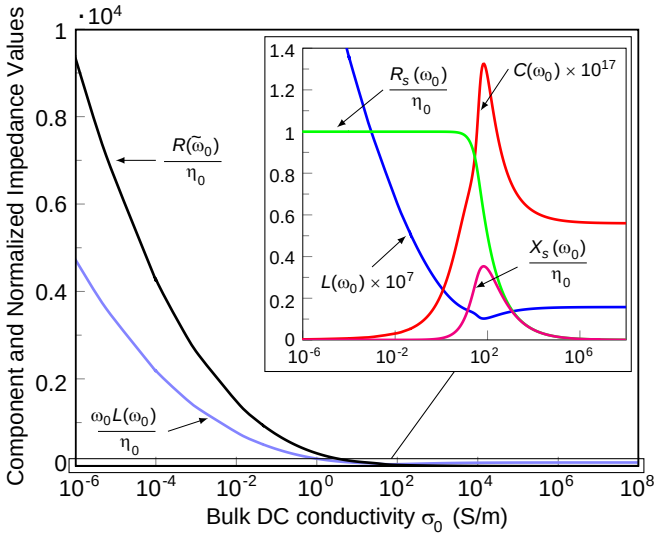

Figure 14. Exact values at resonance for the lumped-element RLC equivalent circuit components and surface impedance, against intrinsic wall conductivity.

4.2. Extended Perturbation Solution

With spherical cavity resonators, it has been found that

$$R\left(\tilde{\omega}_0\right) \sim \xi R_s\left(\omega_0\right) \beta_0^2 S \tag{36}$$

For an air-filled spherical cavity resonator, having a radius of 150 µm, the 1% deviation between the exact (35) and approximation (36) representations of series resistance $R(\tilde{\omega}_0)$ occurs at a bulk DC wall conductivity of $\sim 125\,\mathrm{S/m}$.

Using (24), (30) and (36), the surface resistance at the undamped resonance frequency is approximated by

$$R_s\left(\omega_0\right) \sim 2\omega_0'' \Gamma \sim \left(\frac{\omega_0}{\omega_{\mathrm{I}}}\right) \frac{\eta_0}{Q_u\left(\omega_0\right)} \tag{37}$$

which is now only a function of ω_0, yielding (14b) for unloaded quality factor using our extended perturbation approximation

$$Q_u\left(\omega_0\right) = \frac{\omega_0 L\left(\omega_0\right)}{R\left(\tilde{\omega}_0\right)} \sim \frac{\omega_0 \Gamma}{R_s\left(\omega_0\right)} \tag{38}$$

For an air-filled spherical cavity resonator, having a radius of 150 µm, the 1% deviation between the exact (5) and approximations, using (14) and (29), representations of unloaded quality factor can be determined. It has been found that with traditional perturbation theory (using (14a)), the 1% worst-case threshold for wall conductivity is found at $\sim 1 \times 10^5\,\mathrm{S/m}$ for both driven and undriven cases. However, with our extended perturbation theory (using (14b)), the minimum wall conductivities are extended down to $\sim 130\,\mathrm{S/m}$ and $\sim 1 \times 10^3\,\mathrm{S/m}$, for the driven and undriven cases, respectively. Therefore, with our particular cavity example, the extended perturbation theory can be employed over an extended range of two orders of magnitude in wall conductivity, i.e., not only with "good electrical conductors" (e.g., including carbon).

5. CONCLUSION

Until now, very lossy metal-walled spherical cavity resonators have not been studied. Also, commercial eigenmode solvers have not been stress-tested for their use with very lossy materials. Our paper addresses both issues in an exact and traceable way.

A lossy metal-wall cavity resonator is studied that extends well beyond the limits of perturbation theory. An exact analytical solution was employed for the spherical cavity resonator, having walls transformed from being a PEC to free space, as the intrinsic bulk DC conductivity decreases from infinity down to zero. The resulting model acts as an ideal benchmark reference standard for stress-testing eigenmode solvers, for predicting the eigenfrequency of lossy arbitrary 3D structures. A plane-wave approximation was then derived. Independent full-wave numerical modelling of the spherical cavity resonator was undertaken using eigenmode solvers within two well-known commercial, industry-standard, simulation software packages.

It was found that our plane-wave approximation model accurately characterized the results generated by these solvers when FCB and LIB conditions were employed. However, the IB condition was also accurately characterized by the exact model, but the precise value of complex wave impedance at the wall boundary for the specific resonance mode must first be known *a priori*. This essentially represents a self-fulfilling prophesy. Our stress-testing results have profound implications on the usefulness of these commercial solvers for accurately predicting the eigenfrequencies of lossy arbitrary 3D structures, when even the simplest geometry (i.e., that of the perfect sphere) is considered.

For completeness, an exact series RLC equivalent circuit model is given specifically for the spherical cavity resonator having arbitrary wall losses. This is particularly useful if characterizing resonators can be undertaken without the need for performing electromagnetic calculations. From our RLC model, an extended perturbation model was derived. It is found that our extended perturbation model results in a worst-case 1% error in unloaded quality factor (at the damped resonance frequency) with wall conductivity as low as $\sim 1{,}000\,\mathrm{S/m}$, with an air-filled spherical cavity resonator having a radius of 150 µm. This extends the 1% threshold in wall conductivity down by two orders of magnitude, when compared to traditional perturbation theory (i.e., well beyond the "good electrical conductors" range).

From this study, a deeper insight into the behavior of lossy spherical cavity resonators and commercial eigenmode solvers has been obtained. It is believed that other cavity resonator geometries can be studied, based on the techniques given in this paper. Finally, while eigenmode solvers in HFSS^{TM}and COMSOL have been investigated, similar limitations may be found when stress-testing other similar software packages or in-house developed codes.

ACKNOWLEDGMENT

The authors would like to acknowledge Prof. Makoto Kuwata-Gonokami and Dr. Takuya Higuchi, from the Photon Science Center at the University of Tokyo, and also Prof. M. Tavares de Melo, from the Department of Electronics and Systems at the Federal University of Pernambuco, for their helpful suggestions.

REFERENCES

1. Hansen, W. W., "A type of electrical resonator," *J. Appl. Phys.*, Vol. 9, No. 10, 654–663, Oct. 1938.
2. Barrow, W. L. and W. W. Mieher, "Natural oscillations of electrical cavity resonators," *IRE Proc.*, Vol. 28, No. 4, 184–191, Apr. 1940.
3. Gallagher, S. and W. J. Gallagher, "The spherical resonator," *IEEE Trans. Nucl. Sci.*, Vol. 32, No. 5, 2980–2982, Oct. 1985.
4. Nepal, N., Y. K. Kim, Y. S. Bae, I. S. Ko, M. H. Cho, and W. Namkung, "Design study on standing-wave linear accelerator," *IEEE Proc. PAC 2001*, Vol. 4, 2802–2804, Jun. 2001.
5. Shvets, G., "Optical polarizer/isolator based on a rectangular waveguide with helical grooves," *Appl. Phys. Lett.*, Vol. 89, No. 14, 141127, Oct. 2006.
6. Balanis, C. A., *Advanced Engineering Electromagnetics*, Wiley, 1989.
7. Otter, W. J., S. M. Hanham, N. M. Ridler, G. Marino, N. Klein, and S. Lucyszyn, "100 GHz ultra-high Q-factor photonic crystal resonators," *Sensors and Actuators A: Physical*, Vol. 217, 151–159, Sep. 2014.
8. Papantonis, S., N. M. Ridler, and S. Lucyszyn, "Rectangular waveguide enabling technology using holey surfaces and wire media metamaterials," *Sensors and Actuators A: Physical*, Vol. 209, 1–8, Mar. 2014.
9. Maier, S. A., *Plasmonics: Fundamentals and Applications*, Springe, 2007.
10. Papantonis, S., S. Lucyszyn, and E. Shamonina, "Dispersion effects in Fakir's bed of nails metamaterial waveguides," *J. Appl. Phys.*, Vol. 115, No. 5, 054903, Feb. 2014.
11. Choi, J. Y. and S. Lucyszyn, "HFSS modelling anomalies with electrically thin-walled metal-pipe rectangular waveguide simulations," *10th IEEE High Frequency Postgraduate Student Colloquium (10th HF-PgC) Digest*, 95–98, Leeds, Sep. 2005.
12. Episkopou, E., S. Papantonis, W. J. Otter, and S. Lucyszyn, "Defining material parameters in commercial EM solvers for arbitrary metal-based THz structures," *IEEE Trans. Terahertz Sci. Technol.*, Vol. 2, No. 4, 513–524, Sep. 2012.
13. Slater, J. C., "Microwave electronics," *Rev. Mod. Phys.*, Vol. 18, No. 4, 441–512, Oct. 1946.
14. Hadidi, A. and M. Hamid, "Analysis of a cylindrical cavity resonator with absorbing wall," *Int. J. Electronics*, Vol. 63, No. 3, 435–442, Mar. 1987.
15. Gastine, M., L. Courtois, and J. L. Dormain, "Electromagnetic resonances of free dielectric spheres," *IEEE Trans. Microw. Theory Techn.*, Vol. 15, No. 12, 694–700, Dec. 1967.
16. Collin, R. E., *Field Theory of Guided Waves*, 2nd Edition, IEEE Press, 1991.
17. Lucyszyn, S. and Y. Zhou, "Engineering approach to modelling frequency dispersion within normal metals at room temperature for THz applications," *Progress In Electromagnetics Research*, Vol. 101, 257–275, 2010.
18. Zhou, Y. and S. Lucyszyn, "Modelling of reconfigurable terahertz integrated architecture (RETINA) SIW structures," *Progress In Electromagnetics Research*, Vol. 105, 71–92, 2010.

19. Jiang, J., R. Saito, A. Grueneis, G. Dresselhaus, and M. S. Dresselhaus, "Electron-photon interaction and relaxation time in graphite," *Chem. Phys. Lett.*, Vol. 392, 383–389, 2004.
20. http://www.ansys.com/products/hf/hfss/.
21. http://www.comsol.com/.
22. Pozar, D. M., *Microwave Engineering*, 2nd Edition, Wiley, 1998.
23. Zhou, Y. and S. Lucyszyn, "HFSS^{TM} modelling anomalies with THz metal-pipe rectangular waveguide structures at room temperature," *PIERS Online*, Vol. 5, No. 3, 201–211, 2009.
24. Ramo, S., J. R. Whinnery, and T. Van Duzer, *Fields and Waves in Communication Electronics*, 3rd Edition, Wiley, 1994.
25. Montgomery, C. G., R. H. Dicke, and E. M. Purcell, *Principles of Microwave Circuits*, Chapter 7, McGraw-Hill, 1948.